Neuron, Volume *101*

Supplemental Information

Functional Synaptic Architecture of Callosal Inputs in Mouse Primary Visual Cortex

Kuo-Sheng Lee, Kaeli Vandemark, Dávid Mezey, Nicole Shultz, and David Fitzpatrick

Supplemental information for:

Functional synaptic architecture of callosal inputs in mouse primary visual cortex

Kuo-Sheng Lee[1,2,3], Kaeli Vandemark[1], Dávid Mezey[1], Nicole Shultz[1], David Fitzpatrick[1,4]

[1]Max Planck Florida Institute for Neuroscience, 1 Max Planck Way, Jupiter, FL 33458, USA

[2]Integrative Biology and Neuroscience Graduate Program,

[3]International Max Planck Research School for Brain and Behavior, Florida Atlantic University, Jupiter, FL 33458, USA

Supplemental Results

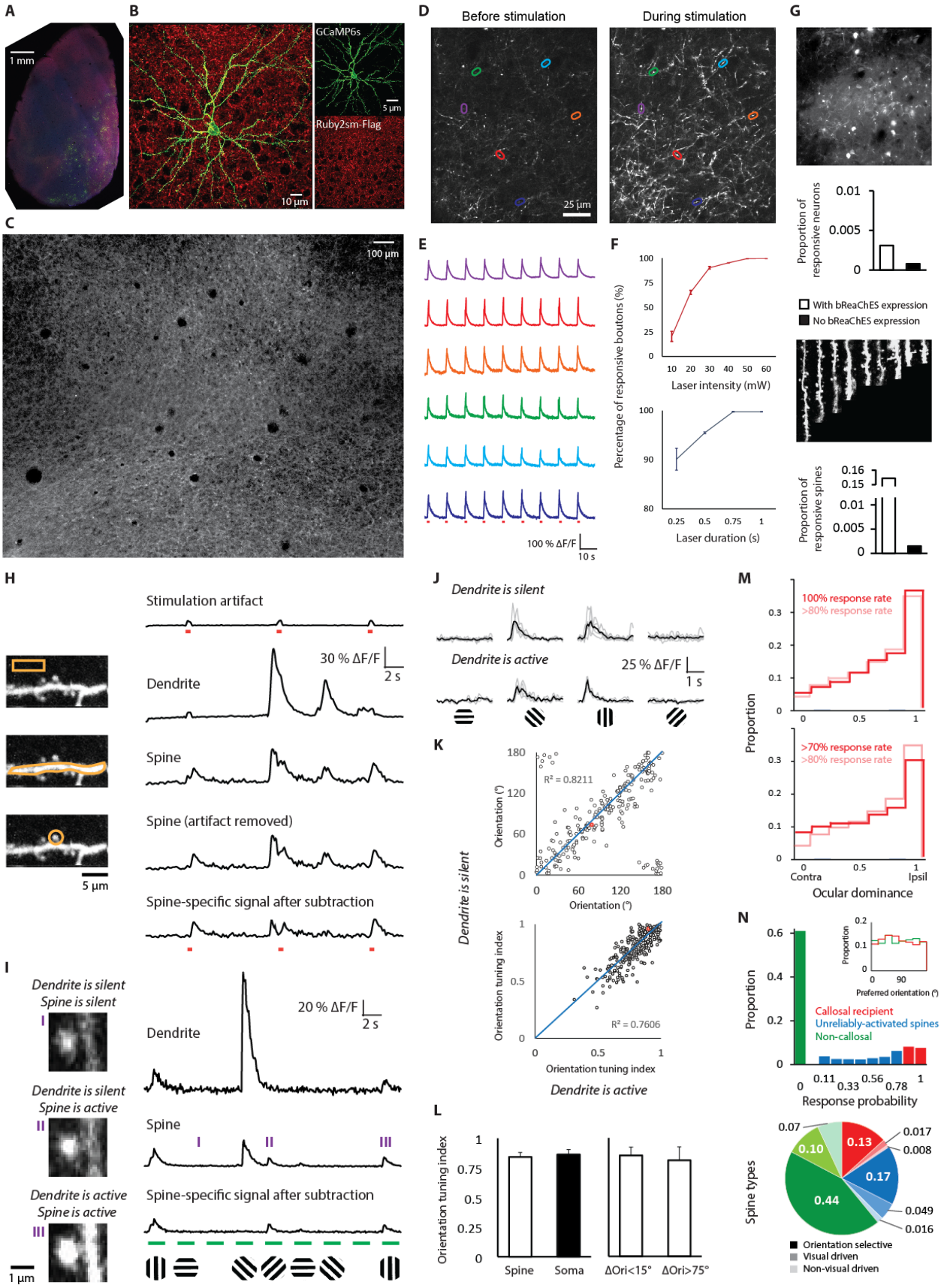
A
1 mm
B
GCaMP6s
5 µm
Ruby2sm-Flag
10 µm
C
100 µm
D
Before stimulation
During stimulation
25 µm
E
100 % ΔF/F
10 s
F
Percentage of responsive boutons (%)
Laser intensity (mW)
Laser duration (s)
G
Proportion of responsive neurons
With bReaChES expression
No bReaChES expression
Proportion of responsive spines
H
Stimulation artifact
30 % ΔF/F
2 s
Dendrite
Spine
Spine (artifact removed)
Spine-specific signal after subtraction
5 µm
I
Dendrite is silent
Spine is silent
Dendrite is silent
Spine is active
Dendrite is active
Spine is active
20 % ΔF/F
2 s
Dendrite
Spine
Spine-specific signal after subtraction
1 µm
J
Dendrite is silent
Dendrite is active
25 % ΔF/F
1 s
K
R² = 0.8211
Orientation (°)
Dendrite is silent
R² = 0.7606
Orientation tuning index
Dendrite is active
L
Orientation tuning index
Spine
Soma
ΔOri<15°
ΔOri>75°
M
100% response rate
>80% response rate
>70% response rate
>80% response rate
Proportion
Contra
Ipsil
Ocular dominance
N
Proportion
Preferred orientation (°)
Callosal recipient
Unreliably-activated spines
Non-callosal
Response probability
Spine types
0.07
0.10
0.13
0.017
0.008
0.17
0.44
0.049
0.016
Orientation selective
Visual driven
Non-visual driven

Supplemental Figure 1 (related to Figure 1): Channelrhodopsin-2-assisted synaptic mapping (CRASM) and spine type categorization.

(A) Epifluorescence image of a tangential brain slice (50 um) containing Layer 2/3 neurons sparsely labeled with GCaMP6s (green) and callosal projections labeled with Ruby2sm-Flag (Red).

(B) Confocal images of a layer 2/3 neuron expressing GCaMP6s (green) and axons expressing Ruby2sm-Flag (Red). No cell bodies labeled with Ruby2sm-Flag were observed.

(C) Representative epifluorescence image of callosal projections labeled with bReaChES. Retrograde labeling of cell bodies by bReaCHES was not observed.

(D) Fluorescence of axonal boutons consistently and dramatically increased during the laser stimulation of fast red-activated channelrhodopsin (bReaChES). Both images are adjusted with the same brightness and contrast.

(E) Within the six example boutons, an increase in fluorescence always follows short laser stimulation (red line segments, 50mW).

(F) Laser intensity-dependent and duration-dependent curves for bouton activation were measured by fixing laser duration at 0.5 s or laser intensity at 40 mW (n = 266 boutons, 3 mice). Error bars represent SEM.

(G) Top: Two-photon imaging of cell bodies of layer 2/3 V1 neurons labeled with GCaMP6s while laser stimulation was delivered to contralateral V1. Stimulus-responsive neurons were extremely rarely observed, whether with (n = 1387 cells, 2 mice) or without bReaChES expression (n = 1229 cells, 1 mouse). Bottom: Two-photon imaging of dendrites of a single layer 2/3 neuron labeled with GCaMP6s while laser stimulation was delivered to contralateral V1. Stimulus-responsive spines were occasionally observed in the experiments with bReaChES expression (n = 2645 spines, 12 mice), but nearly absent in the animal without bReaChES expression (n = 882 spines, 1 mouse).

(H) Left: A dendritic segment labeled with GCaMP6s within the two-photon field of view recorded from a single experimental session. Orange outlines denote regions of interest that are the basis for the fluorescence traces shown on the right. Right: Postsynaptic activity from a single example spine was isolated by subtracting the stimulation artifact and component of the signal from the dendritic shaft. Red line: Duration of light stimulus.

(I) Left: Fluorescence dynamics of an example dendritic spine. Right: Visual-evoked activity from the example spine was isolated by subtracting the component of the signal from the dendritic shaft. Green line: Duration of visual stimulation.

(J) Comparing the average responses (black) to the oriented grating stimuli of a single example spine in the presence or absence of dendritic activity. Preferred orientation and tuning index of the spine were nearly identical. Gray lines indicated single trial activities.

(K) Comparing preferred orientation and tuning index of spines while dendrite is silent or active (n = 238 spines, 8 mice, $P<0.001$). Red dot is the example in (J).

(L) Left: Spines showed high orientation tuning index comparable to V1 excitatory neurons (n = 658 spines, 8 mice; n = 284 cells, 2 mice; Wilcoxon rank-sum, $P = 0.75$). Right: When comparing the tuning index of spines with orientation preference similar to the soma (ΔOripref < 15°, n = 287 spines, 8 mice) with that of spines whose orientation preference was orthogonal to the soma (ΔOripref > 75°, n = 97 spines, 8 mice), the tuning index was not significantly different between the two groups (Wilcoxon rank-sum, $P = 0.18$). This is further evidence to support the fidelity of the subtraction method, indicating that it does not generate aberrant orientation tuned responses.

(M) Distribution of dendritic spine ocular dominance values as a function of response reliability following optogenetic activation. Top: There is no statistical difference in ocular dominance distribution using a response reliability criterion of 100% (n = 155 spines, 12 mice) versus 80% (n = 342 spines, 12 mice, $P = 0.87851$, Wilcoxon rank sum test). Bottom: using a response reliability criterion of 70% (n = 454 spines, 12 mice) resulted in a significant difference in the ocular dominance distribution versus 80% reliability criterion (n = 342 spines, 12 mice, $P = 0.02231$, Wilcoxon rank sum test).

(N) Top: Distribution of response probability to laser stimulation for all imaged spines (n = 2645 spines, 12 mice). Spines reliably responding to laser stimulation on more than 80% of trials were considered callosal-recipient spines. Insert: Distribution of orientation preference for callosal spines and non-callosal spines. Bottom: Proportion of different classes of dendritic spines on layer 2/3 neurons, based on their response reliability (color) and visual response properties (lightness, indicated in shades of grey).

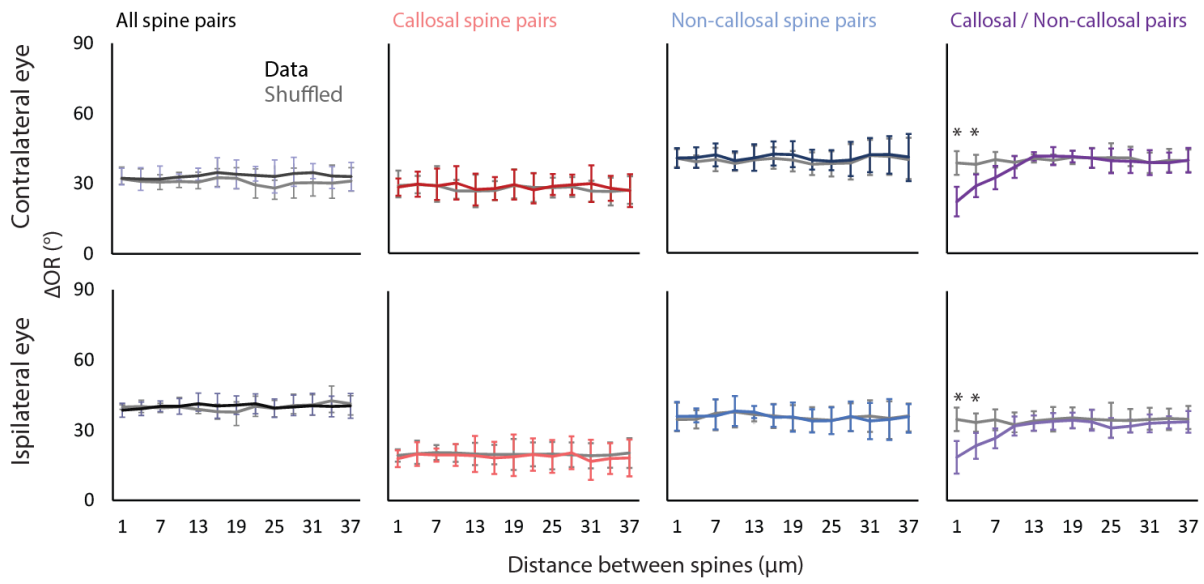

Supplemental Figure 2 (related to Figure 2):. Orientation-preference based functional clustering of callosal and non-callosal spine pairs is robust when shuffling spine preferred orientation only within branches.

When analysis is done by shuffling spines by preferred orientation only within branches, the relationship between orientation preference and distance between spines across different inputs remains unchanged (n = 798 all spine pairs; n = 138 callosal spine pairs; n = 714 non-callosal spine pairs; n = 204 callosal/non-callosal pairs, 129 dendrites, 12 mice). Error bars represent SEM. *, P<0.01, permutation test.

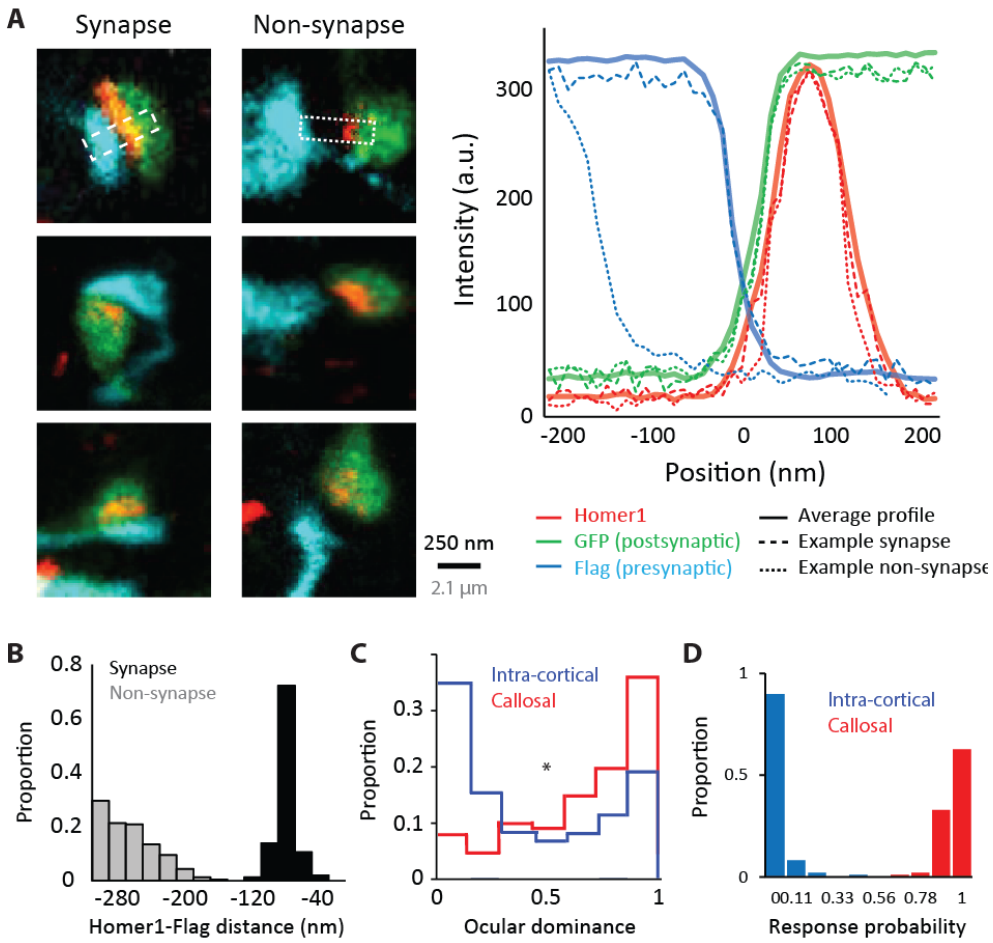

Supplemental Figure 3 (related to Figure 3): Visualizing synaptic contacts of callosal networks with expansion microscopy.

(A) Left: Images of three example synapses and three example non-synapses, individually composed of an axonal bouton (cyan), dendritic spine (green), and postsynaptic density (red). Right: Comparing the intensity profiles of the example synapse and non-synapse to the average intensity profile of 121 total synapses. The distance between Flag (presynaptic marker) and Homer1 (postsynaptic density) could be used to distinguish the synapse and non-synapse. Scale bars are provided both in physical size post-expansion (gray) and back-calculation with expansion factor (black).

(B) This imaging method displays the distance between Homer1 and Flag, showcasing clarity in identifying the synapse and non-synapse (n = 411 synapses, 411 non-synapses, 6 mice).

(C) Distribution of ocular dominance values for intra-cortical (n = 312 spines, 6 mice) and callosal-recipient spines

(n = 71 spines, 6 mice). *, P<0.001, Wilcoxon rank sum test.

(D) The distribution of response probability following laser stimulation in the CRASM experiment of callosal (n = 59 spines, 1 mouse) or intra-cortical (n = 243 spines, 1 mouse) recipient spines. Anatomical results validated the stimulus reliability criterion (80%) used in CRASM experiments.

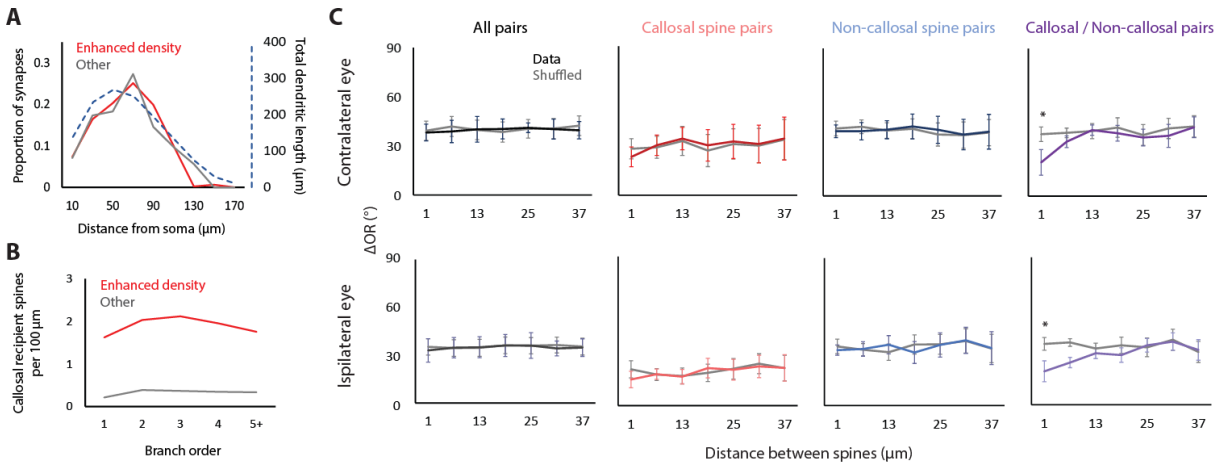

Supplemental Figure 4 (related to Figure 4):. Orientation-preference based functional clustering of callosal and non-callosal spine pairs is present in branches with enhanced density of callosal-recipient spines.

(A) Summary of the locations of all callosal spines on either dendritic branches receiving enhanced density of callosal inputs (red line) or other dendritic branches (gray line) (n = 12 cells, 12 mice). Dashed line indicates the average summed dendritic lengths in increasing distance away from the soma (right y-axis), which is highly similar to the distribution of callosal inputs.

(B) Summary of the density of the callosal spines on the dendritic branches with different branch orders (n = 12 cells, 12 mice).

(C) When analysis is restricted to dendritic branches receiving a significantly enhanced density of callosal inputs derived from CRASM, the relationship between orientation preference and spine pair distance across different inputs remains unchanged (n = 1744 all spine pairs; n = 186 callosal spine pairs; n = 1257 non-callosal spine pairs; n = 394 callosal/non-callosal pairs, 28 dendrites, 12 mice). Error bars represent SEM. *, P<0.01, permutation test.